The Solar Rotation and Its Evolution during Cycle 23

Sylvain G. Korzennik[1] and Antonio Eff-Darwich[2]

[1]*Harvard-Smithsonian Center for Astrophysics, Cambridge, MA 02138, USA*

[2]*Instituto de Astrofisica de Canarias / Universidad de La Laguna, Tenerife, Canary Islands E-38205, Spain*

Abstract. We present the most exhaustive and accurate inferences of the internal solar rotation rate and its evolution during solar cycle 23. A full solar cycle of Michelson Doppler Imager (MDI) observations has been analyzed using our state of the art fitting methodology. Time series of various lengths have been fitted, from a single 4608-day long epoch (64×72 day or 12.6 year) down to 64 separate segments for the traditional 72-day long epochs. We used time series of spherical harmonic coefficients computed by the MDI group but using an improved spatial decomposition. This decomposition now includes our best estimate of the image plate scale and of the MDI instrumental image distortion. The leakage matrix used for the fitting includes the effect of the distortion of the eigenfunctions by the solar differential rotation, and the undistorted leakage matrix was itself carefully reviewed and independently recomputed. Rotation inversions were carried out for all the available mode sets for that epoch and all available segments, including the MDI and Global Oscillation Network Group (GONG) pipeline sets. The improved inversion method we used is an iterative methodology based on a regularized least-squares. It implements a model grid optimization derived from the actual information in the input set. This optimized model grid is itself irregular, namely with a variable number of latitudes at different depths. We present the most accurate mean rotation rate, to date. We also focus on the change of the rotation rate with activity levels and how well these changes are assessed at high latitudes and below the surface, down to the base of the convection zone.

1. Introduction

Both GONG and MDI have by now acquired more than 15 years of observations. Still, the GONG pipe-line uses a two-decade-old mode fitting procedure (Anderson et al. 1990), where "individual" modes are independently fitted without any inclusion of the leakage matrix information (as a result these are in fact more often blends than modes). The fitted profile is a symmetric Lorentzian, and the time series are broken up in 108-day long overlapping epochs, 36 days apart. As for MDI, the fitting pipe-line is based on Schou (1992), with some recent improvements (Larson & Schou 2008). The procedure fits singlets, not multiplets, and uses a polynomial expansion in *m* to represent the frequency splittings. The MDI procedure fits 72-day long time series and makes explicit use of a leakage matrix. Recent improvements to the MDI procedure include (a) an improved spatial decomposition – to correct for the image plate scale and the image distortion, (b) an effective leakage matrix that incorporates the effect of the dis-

tortion of the eigenvalues by the differential rotation (Woodard 1989) and (c) fitting to a symmetric or asymmetric mode profile.

Results presented here are also derived from an independent fitting methodology (Korzennik 2005, 2008). The key elements of this method are (a) the inclusion of the complete leakage matrix – distortion by differential rotation included, (b) fit to an asymmetric profile, (c) the use of an optimal multi-tapered spectral estimator, (d) fitting all multiplets simultaneously – i.e., all m for a given n, ℓ, (d) a sanity rejection – a Signal-to-Noise Ratio (SNR) based fitting threshold, (e) mode contamination via an iterative process, and (f) the fitting of time-series of varying lengths. This method was applied to improved MDI spherical harmonic coefficients, namely coefficients resulting from the spatial decomposition that incorporates the correct plate scale and both components of the instrumental image distortion. The fitting was carried out for $64\times, 32\times, 16\times, 8\times, 4\times \& 2\times72$-day long, overlapping time-series, as well as 1×72-day long non-overlapping epochs, for the 1996.05.01 to 2009.07.16 period.
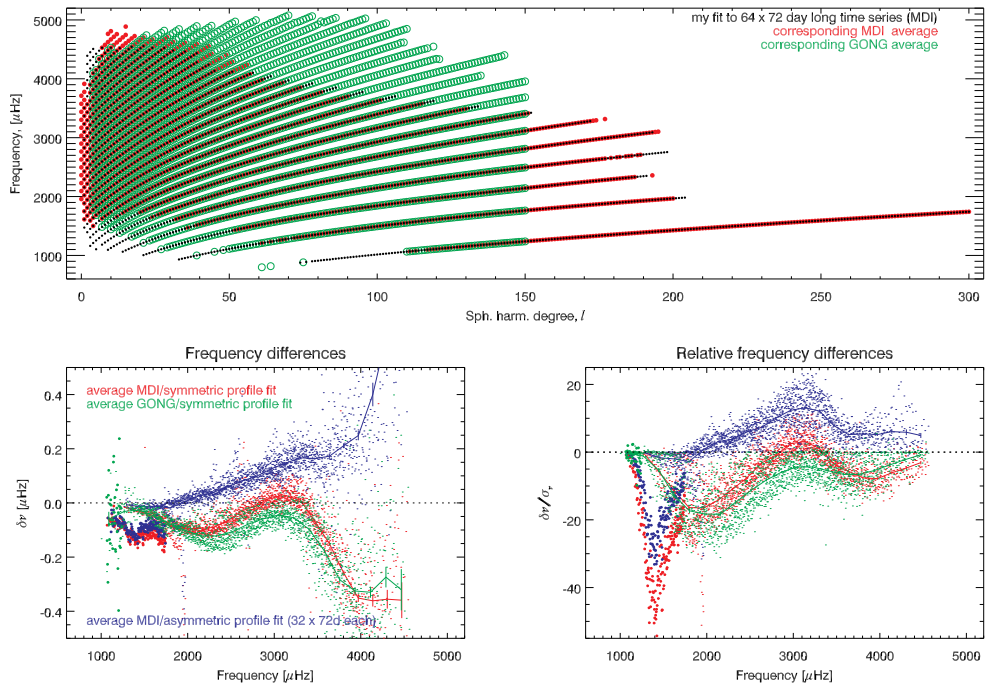
2. Fitting Results

Figure 1.   Comparison of fitted frequencies (singlets): top panel shows the coverage in the $\ell - \nu$ plane, bottom panels shows frequency and relative frequency differences (i.e., differences divided by the uncertainty). Black dots correspond to modes fitted using our independent fitting methodology, applied to 64×72 day long time series, the red and green dots correspond to MDI and GONG pipe-line fitting respectively, while the blue dots correspond to MDI revised fitting, using an asymmetric profile (and for the corresponding 64×72 day long time series). The large dots correspond to the f-modes, the curves are corresponding binned values.
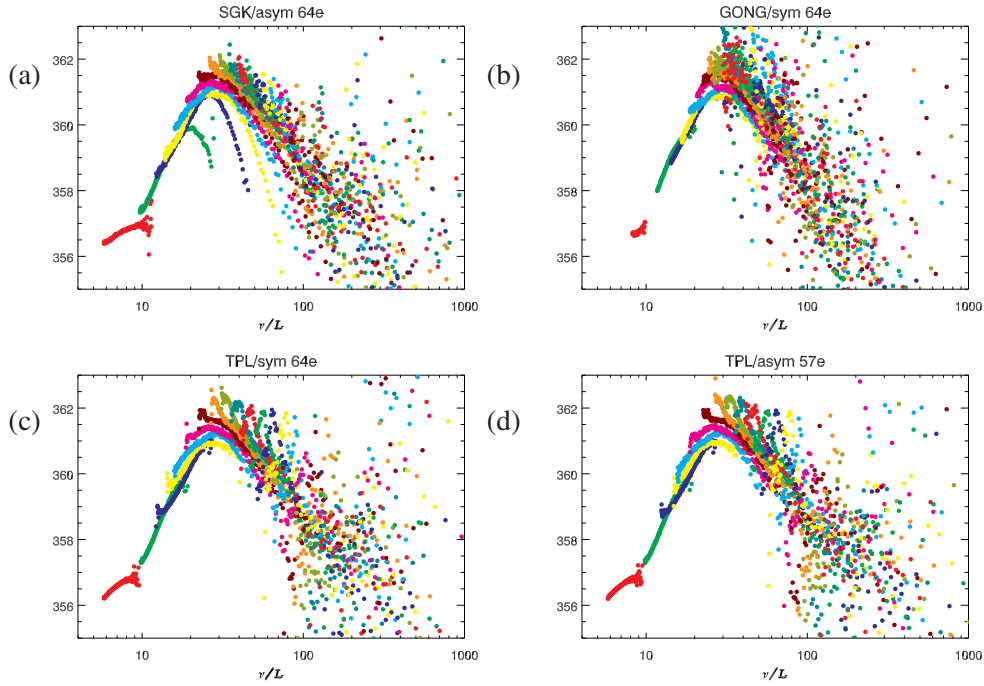
Figure 2. Comparison of the frequency splitting leading Clebsch-Gordan coefficient derived from four mode fitting procedure: (a) results from using our independent fitting methodology, (b) GONG pipe-line, (c) MDI improved symmetric fit, and (d) MDI improved asymmetric fit.

Figure 1 compares frequencies resulting from the various mode fitting techniques (singlets), while Fig. 2 compares rotational splittings, computed using the longest fitted period (62×72 day long, or 12.6 year). Note the systematic offset between the frequencies, even when comparing asymmetric fits. Splitting comparisons display systematic offsets, at the 0.5 to $1.4\,\sigma$ level.

2.1. Mode Attrition

Figure 3 shows the mode attrition of the different fitting methods, namely how often the same mode is successfully fitted at each epoch. Note how the character of the attrition changes with each fitting procedure. The problem associated with mode attrition is easily illustrated from simple considerations associated with inverse theory.

A generic inverse problem is usually defined as

$$y_i = \int K_i \, x(p) \, dp \qquad (1)$$

and is, in most cases, a singular problem that requires regularization –usually a smoothness constraint– to infer an estimate of the solution, i.e.,

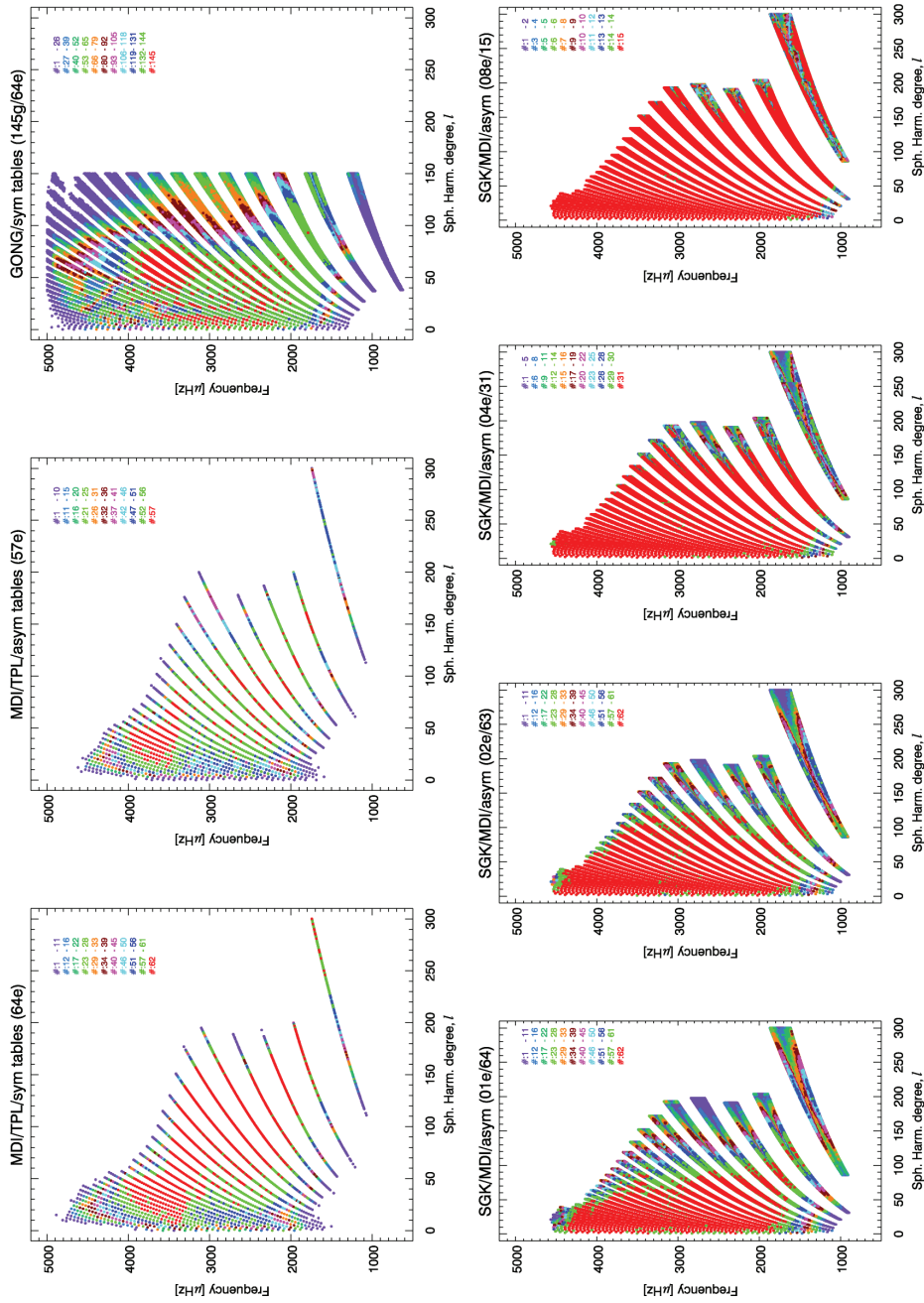$$\hat{x}(p_k) = \int R(p, p_k) \, x(p) \, dp, \qquad (2)$$

Figure 3. Mode attrition in the $\ell - \nu$ plane. The color represents how often a mode is fitted, with red indicating all the time (100%), green 90%, etc. The top panels correspond to MDI improved symmetric and asymmetric fit and GONG pipe-line fit. The bottom panels correspond to our independent fitting methodology, for 1×, 2×, 4×, 8 × 72 day long time series (left to right).
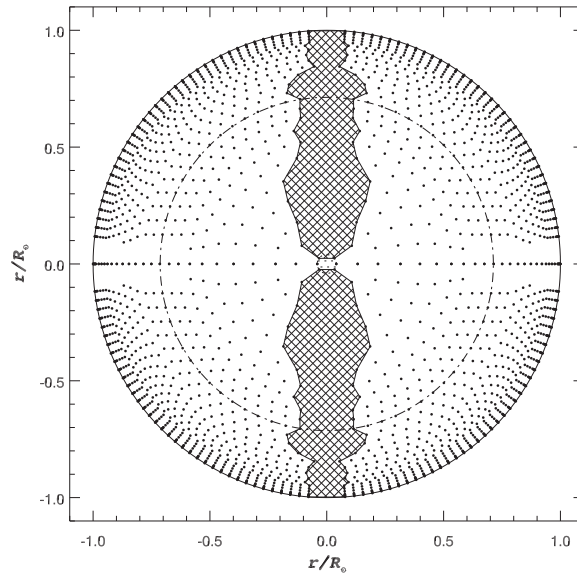
Figure 4.   Non-uniform model grid for the inversions, derived using an optimization based on the available input set. The hatched area corresponds to the region where the inversion is unable to derive a localized estimate of the solution, given the input set and its precision.

where R is known as the resolution kernel, a function that relates the estimate, $\hat{x}$, derived at the location p_k, to the underlying model, x. A well localized estimate will correspond to a resolution kernel close to a "delta" distribution centered on p_k. The resolution kernel, R, depends on the input set used for the inversion. In the case of the solar rotation, the inverse problem is

$$\delta v_{n,\ell,m} = \iint K_{n,\ell,m}(r,\theta)\,\Omega(r,\theta)\,dr\,d\theta, \tag{3}$$

where the input set is defined by $\{n, \ell, m\}$ or $\{n, \ell, a_i\}$ (when using splitting coefficients). Any temporal changes in the input set affect R, hence $\hat{x}$, the estimate of the solution. To avoid injecting apparent changes in the inverted estimates associated with changes in resolution we invert constant input sets. Fitting methodologies that produce high attrition severely reduce the constant set, while using at each epoch all the fitted modes results in ambiguous estimates of changes with epoch.

3.   Inversion Results

3.1.   The Inversion Method

The rotational splittings, based on individual modes when available, were inverted using a modified regularized least-squares method (Eff-Darwich et al. 2008). This method uses an iterative approach to derive an optimal model grid based on the available input set. That model grid is non-uniform, namely a grid whose number of latitudes varies with radius, as presented in Fig. 4.
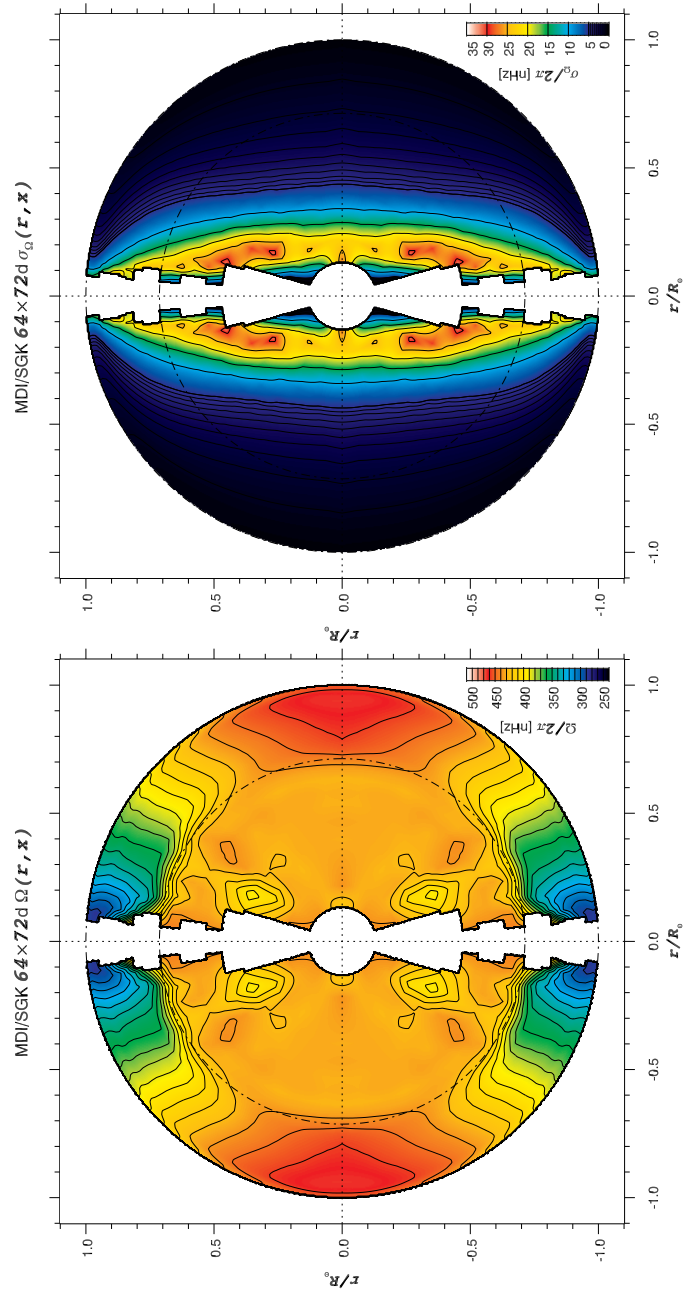
Figure 5.   Mean rotation profile (left) and its formal precision (right) for Cycle 23. This profile is inverted from frequency splittings, not splitting coefficients, resulting from fitting 64 × 72 day long time series using our independent methodology.

3.2.   Inversion of 12.6 Year-long Data Set

Figure 5 presents the best to date mean rotation profile for Cycle 23. That profile is derived from frequency splittings (not splitting coefficients) resulting from fitting
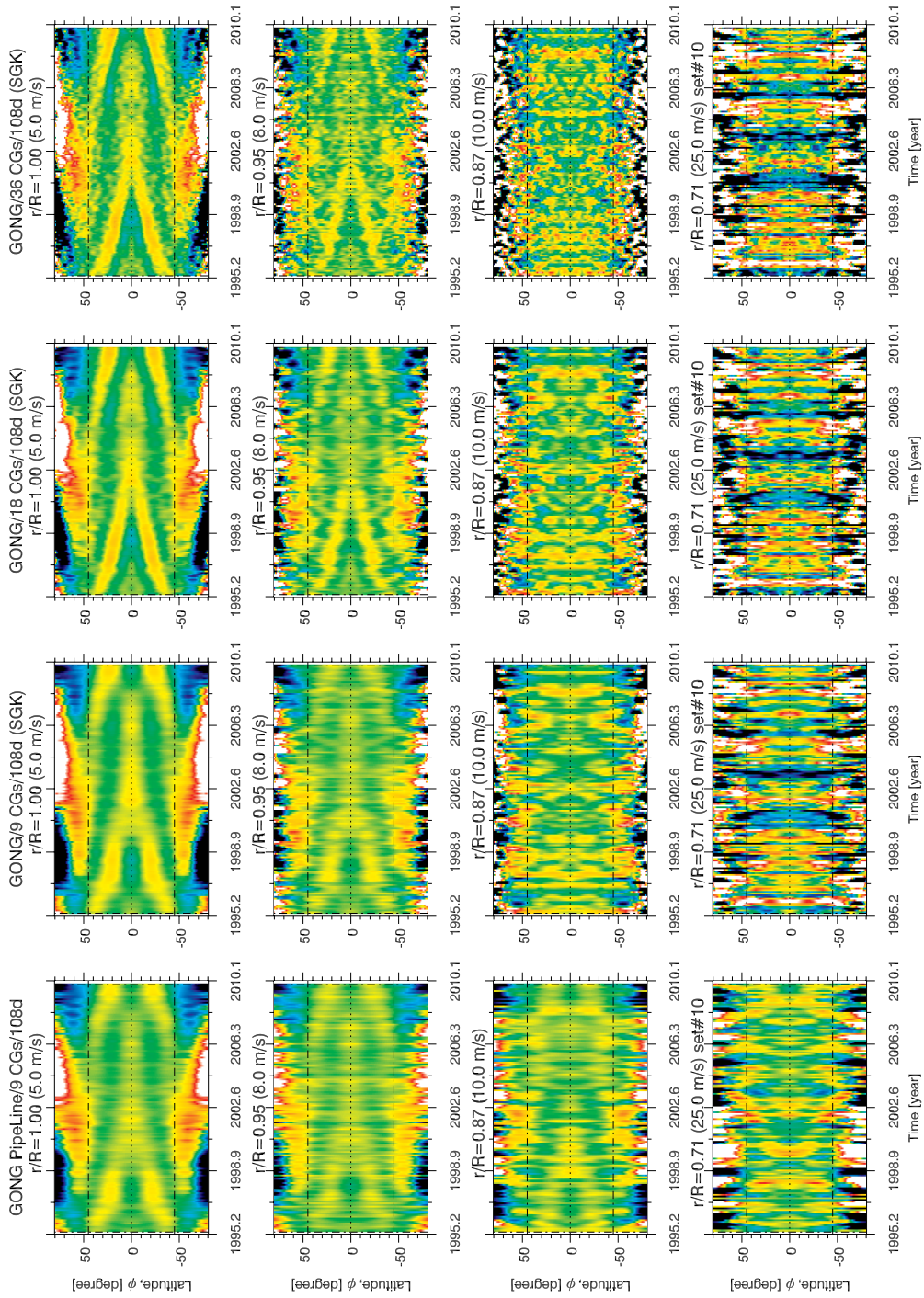
Figure 6. Rotation rate change as a function of time and latitude derived from inversions using Clebsch-Gordan coefficients, at four depths ($r/R = 1, 0.95, 0.87, 0.71$ top to bottom) and using either the GONG pipeline 9 terms expansion, or our fit to GONG frequency tables using 9, 18 or 36 terms (left to right).
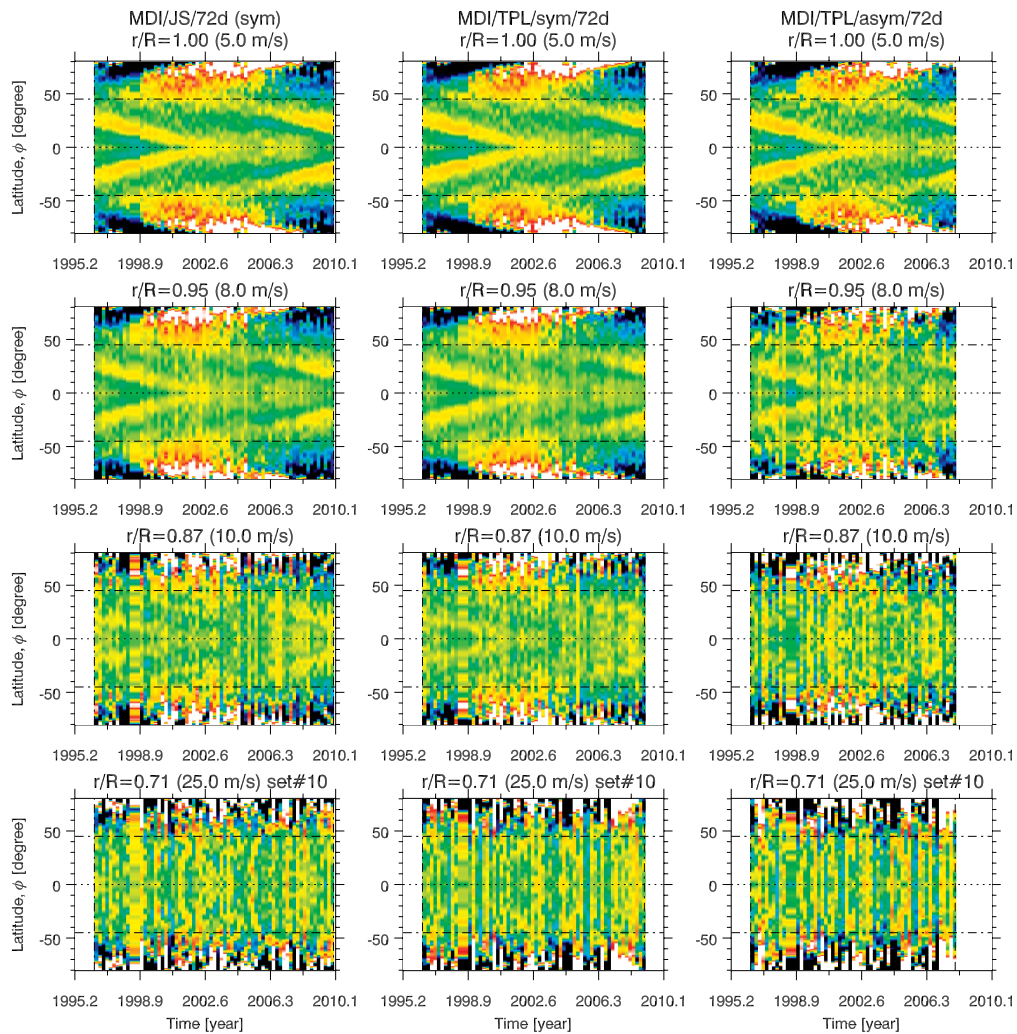
Figure 7.   Rotation rate change as a function of time and latitude derived from inversions using Clebsch-Gordan coefficients, same four depths, using MDI's tables: standard & improved symmetric and asymmetric profiles – left to right.
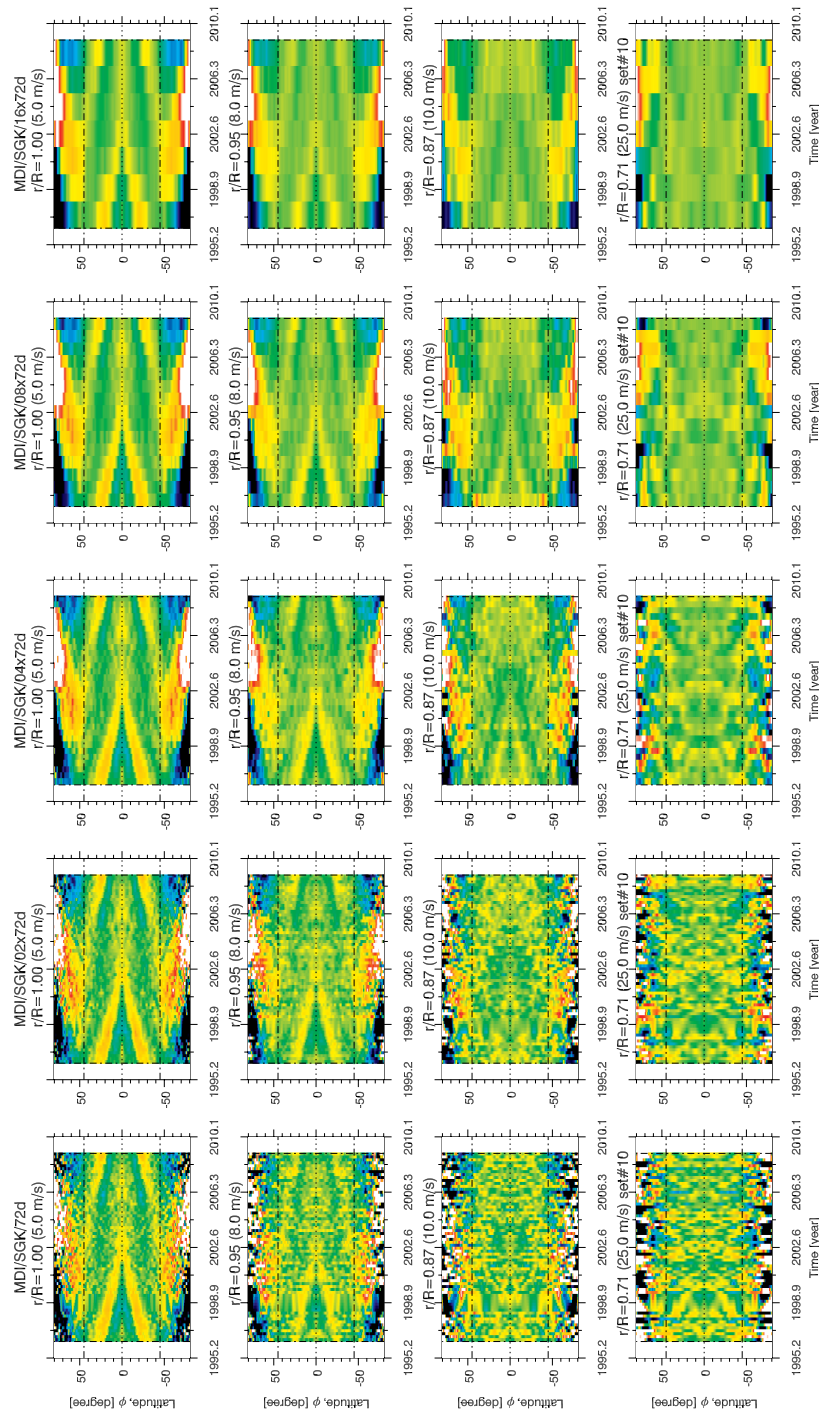
Figure 8.   Rotation rate change as a function of time and latitude derived from inversions using frequency splitings (not coefficients), same four depths, using results of our independent fitting methodology to MDI's 1×, 2×, 4×, 8× & 16×72 day long epochs (left to right).

64×72 day long time series. The figure shows a radiative core that rotates at a nearly constant rate, with the differential rotation confined to the convective envelope. The precision of the inverted profile, indicated by the formal uncertainties shown on that same figure, is below the 1% level, but quickly rises for estimates close to the rotation axis.

3.3.   Rotation Rate Changes

Changes in the rotation rate, as a function of time and latitude are presented in Figs. 6 to 8, using splittings computed by the GONG pipe-line, the improved MDI pipe-line and our own independent methodology, at four depths in the convection envelope ($r/R = 1.00 - 0.71$). Figs. 6 to 7 show changes derived from using slightly different estimates of the rotational splittings generated by the GONG and MDI pipe-lines, while Fig. 8 shows rotation rate changes derived from our independent fitting methodology when applied to time series of varying length (i.e., 1×, 2×, 4×, 8× & 16×72 day long epochs).

4.   Conclusions

While some issues still remain unsolved in our mode fitting methodologies, we have infered a mean solar rotation for Cycle 23 based on fitting a very long time-series. This results in an improved precision, resolution and extent. The determination of significant changes of the rotation rate with time is easy at the surface and at low latitudes. It becomes challenging when extended to high latitudes or down to the base of the convection zone, while it remains difficult to push inferences to the radiative interior, without using very long time series and thus reducing the temporal resolution. A more consistent picture, especially at larger depths, emerges when using results derived from fitting longer time series.

References

Anderson, E. R., Duvall, T. L., Jr., & Jefferies, S. M. 1990, ApJ, 364, 699
Eff-Darwich, A., Korzennik, S. G., Jiménez-Reyes, S. J., & García, R. A. 2008, ApJ, 679, 1636
Korzennik, S. G. 2005, ApJ, 626, 585
— 2008, J. Phys.: Conf. Ser., 118, 012082
Larson, T. P., & Schou, J. 2008, J. Phys.: Conf. Ser., 118, 012083
Schou, J. 1992, Ph.D. Thesis, Aarhus University
Woodard, M. F. 1989, ApJ, 347, 1176